Energetics of long internal gravity waves in large lakes

Jason P. Antenucci[1] *and Jörg Imberger*

Department of Environmental Engineering, Centre for Water Research, University of Western Australia, Nedlands, 6907 Australia

Abstract

An analytical model is used to determine dispersion relations and the ratio of potential to kinetic energy in linear basin-scale internal waves in lakes affected by the earth's rotation. It is shown that the wave frequency and energy partitioning in elliptic lakes are dependent only on the direction of propagation relative to the earth's rotation, the aspect ratio, the horizontal mode (azimuthal and radial), and the Burger number ($S_i = c_i/Lf$, where c_i is the non-rotating phase speed, L is a length scale that characterizes the lake dimension, and f is the Coriolis parameter). For the cyclonic (rotating in the same direction as the earth's rotation), lowest radial mode (a Kelvin wave for small S_i and a Poincaré wave for large S_i), the total potential to kinetic energy ratio was always greater than unity for all azimuthal modes. For all other radial modes (Poincaré waves for all S_i), both cyclonic and anticyclonic, the ratio is substantially less than unity, especially as the Burger number decreases. The results demonstrate that basin-scale Poincaré waves follow the same rotation-gravity balance as unbounded plane progressive Poincaré waves, in which rotation plays an increasingly important role as the Burger number decreases. The solutions are applied to field experiments conducted in Lake Kinneret (Israel) to determine the dissipation timescale of the basin-scale internal waves. It is further shown that features of the spatial structure of isopycnal displacement and velocity scales may be inferred from a single station that measures potential energy fluctuations.

The response of a stratified lake to wind forcing is a topic that has received much attention. Some fraction of the energy input by the wind goes into generating internal waves, with basin-scale waves containing the most energy and responsible for transporting mass and momentum over large scales (Imberger 1998). The total energy in the internal wave field is of particular interest, especially when determining the efficiency of energy transfer from the wind to internal waves or when trying to determine the decay timescale of the internal wave field.

In nonrotating systems, internal wave energy is partitioned equally between kinetic and potential forms (Gill 1982). We refer to partitioning as the average potential energy in the wave over one period, divided by the average kinetic energy over one period. The introduction of rotation (Gill 1982) alters the equi-partitioning of energy. For linear progressive waves in a laterally unbounded, rotating system, the ratio of potential to kinetic energy is

$$\frac{\text{PE}}{\text{KE}} = \frac{\omega^2 - f^2}{\omega^2 + f^2},$$ (1)

where ω is the angular frequency of the wave motion and f is the inertial frequency. These waves are known as plane progressive Poincaré waves (Gill 1982) or inertia-gravity waves (Cushman-Roisin 1994). As the wave frequency approaches the inertial frequency, the kinetic energy signal dominates and particle orbits trace out inertial circles (Gill 1982). At high frequency, the waves behave as gravity waves, with the ratio approaching unity.

The relationship (1) holds for waves in laterally unbounded systems, being applicable when the wavelength of the waves is much smaller than the basin scale. In lakes, internal wave activity is generally dominated by basin-scale modes (Mortimer 1952; Antenucci et al. 2000). In a nonrotating system, the partitioning of energy between potential and kinetic forms in basin-scale waves is equal. The total energy in an internal wave can therefore be calculated by simply doubling the energy determined from potential energy measurements, which are typically far simpler to make than the velocity measurements required to determine the kinetic energy.

The earth's rotation starts to affect the dynamics of internal gravity waves when the basin dimension approaches the internal Rossby radius, defined as c/f, the ratio of the nonrotating phase speed c to the inertial frequency f (twice the rate of rotation of the earth at the latitude of the lake). In midlatitude lakes, this length scale is approximately 5 km. The effect of rotation is to change the character of basin-scale internal waves, such that the crests begin to propagate around the boundaries of a lake, instead of across the lake center, as in the nonrotating case. These waves are generally known as Kelvin and Poincaré waves. The partitioning of energy between potential and kinetic forms in linear basin-scale Kelvin and Poincaré waves has not previously been investigated and is the objective of this paper.

The work was motivated by a need to determine the decay timescale of basin-scale internal waves in large lakes, because they are responsible for much of the transport in lakes with long residence times (Imberger 1994). The first step in calculating a decay timescale was therefore to determine the amount of energy in basin-scale Kelvin and Poincaré waves.

This was done by use of potential energy fluctuations (through temperature measurements) and the ratios of potential to kinetic energy derived from the analysis of linear internal waves in a lake of simplified geometry.

We present solutions for linear long waves in rotating circular and elliptic basins, stratified by three homogenous and inviscid layers, and determine the dispersion relations. We discuss the partitioning of energy integrated over the entire basin, as well as the energy partitioning at a point. An application is made to experiments conducted in Lake Kinneret, to demonstrate how the method may be applied to determine the total energy in a basin-scale wave and to approximate displacement and velocity scales from a single station that measures potential energy fluctuations.

Analytical solutions

Elliptical basin—To determine the energy partitioning for linear basin-scale internal waves in a rotating system, we investigated a rotating elliptical basin of uniform depth, with a stratification of three inviscid homogeneous layers and no mean circulation. This model is an extension of the circular basin model used by Antenucci et al. (2000) to describe the basin-scale internal wave field in Lake Kinneret (Israel). The linear solutions for a single layer in an elliptical basin are given in Jeffreys (1925) and Goldstein (1929). The method of normal modes was used to determine the nonrotating phase speed c_i for particular vertical modes, which are then substituted into the generic single layer problem as outlined below. A major benefit of this approach was that the effect of different vertical modes can be investigated separately. The use of three layers allowed us to also investigate the effect of vertical mode on energy partitioning.

We used plane elliptic coordinates, where ξ is the radial and η the angular coordinate. The linear inviscid normal mode equations of motion in a plane elliptic coordinate system are

$$\frac{\partial U_i^\xi}{\partial t} - fU_i^\eta = -\frac{2gD_i}{\sqrt{\phi^2 - \psi^2}(\cosh 2\xi - \cos 2\eta)}\frac{\partial \pi_i}{\partial \xi}, \quad (1)$$

$$\frac{\partial U_i^\eta}{\partial t} + fU_i^\xi = -\frac{2gD_i}{\sqrt{\phi^2 - \psi^2}(\cosh 2\xi - \cos 2\eta)}\frac{\partial \pi_i}{\partial \eta}, \quad (2)$$

where π_i is the modal pressure, U_i the modal transports, ϕ the major axis half-width, ψ the minor axis half-width, g the gravitational constant, D_i the equivalent depth (the depth of a homogeneous fluid required such that the barotropic long wave phase speed in the homogeneous fluid matches the baroclinic long wave phase speed of the internal wave vertical mode being studied), and the index i individual vertical modes. The wave equation can be written as (Jeffreys 1925)

$$\frac{\partial^2 \pi_i}{\partial \xi^2} + \frac{\partial^2 \pi_i}{\partial \eta^2} + 2q(\cosh 2\xi - \cos 2\eta)\pi_i = 0, \quad (3)$$

where q is defined as

$$q_i = \frac{1 - \psi^2/\phi^2}{4}\left(\frac{\sigma_i^2 - 1}{S_i^2}\right), \quad (4)$$

and $\sigma_i = \omega_i/f$ as the nondimensional frequency, where f is the inertial frequency. The Burger number S_i is defined as in (Pedlosky 1987)

$$S_i = \frac{\sqrt{gD_i}}{Lf} = \frac{c_i}{\phi f}, \quad (5)$$

the ratio of the Rossby radius (c_i/f) to a length scale that characterizes the basin dimension, chosen to be the major axis half-length, following the method of Goldstein (1929). This was called a nondimensional channel width or nondimensional rotational speed of the earth by Csanady (1975).

The modal pressure solution to the wave Eq. 3 is assumed to be separable and of the form (Goldstein 1929)

$$\pi_i = \alpha_n(q)ce_n(\eta, q_i)Ce_n(\xi, q_i)\sin \omega_i t$$
$$+ \beta_n(q)se_n(\eta, q_i)Se_n(\xi, q_i)\cos \omega_i t, \quad (6)$$

where n is the azimuthal mode. The first azimuthal mode is equivalent to one sine wave wrapping around the basin (lines of constant ξ). In the following discussion, we consider only $n = 1$. The solution contains ce and se, the cosine-elliptic and sine-elliptic Mathieu functions. Ce and Se are the modified cosine-elliptic and modified sine-elliptic Mathieu functions, respectively. The coefficients (α_n and β_n) are determined by equating the Mathieu function expansions to 0 (Goldstein 1929).

Application of the boundary conditions of no motion normal to the boundary results in the frequency equation (Goldstein 1929)

$$\sigma_i^2 Ce_1'(\xi_0, q_i)Se_1'(\xi_0, q_i) - Ce_1(\xi_0, q_i)Se_1(\xi_0, q_i) = 0, \quad (7)$$

where ξ_0 [$=\text{atanh}(\psi/\phi)$] is the bounding ellipse and the prime refers to the derivative with respect to ξ. The frequency Eq. 7 is an eigenvalue problem in which the solutions fall into "pairs." The two lowest frequencies represent the fundamental radial modes (half a sine wave across the basin along lines of constant angle), with the lower of these two frequencies representing a cyclonic wave (in the same sense as the rotation—counterclockwise in the northern hemisphere), and the higher of the two frequencies representing an anticyclonic wave. The next "pair" forms the second radial mode solutions (one sine wave across the basin along lines of constant angle), again with the lower of the two frequencies in the pair representing a cyclonic wave.

The modal transport fields for the elliptic case are

$$U_i^\xi = \frac{gD_i}{\omega_i^2 - f^2}\left[\frac{2}{(\phi^2 - \psi^2)(\cosh 2\xi - \cos 2\eta)}\right]^{1/2}$$
$$\times [\omega_i\alpha_1 ce_1(\eta, q_i)Ce_1'(\xi, q_i)\cos \omega_i t$$
$$- \omega_i\beta_1 se_1(\eta, q_i)Se_1'(\xi, q_i)\sin \omega_i t$$
$$+ f\alpha_1 ce_1'(\eta, q_i)Ce_1(\xi, q_i)\sin \omega_i t$$
$$+ f\beta_1 se_1'(\eta, q_i)Se_1(\xi, q_i)\cos \omega_i t], \quad (8)$$

$$U_i^\eta = \frac{gD_i}{\omega_i^2 - f^2}\left[\frac{2}{(\phi^2 - \psi^2)(\cosh 2\xi - \cos 2\eta)}\right]^{1/2}$$
$$\times\, [\omega_i\alpha_1 ce_1'(\eta,\, q_i)Ce_1(\xi,\, q_i)\cos\,\omega_i t$$
$$-\,\omega_i\beta_1 se_1'(\eta,\, q_i)Se_1(\xi,\, q_i)\sin\,\omega_i t$$
$$-\,f\alpha_1 ce_1(\eta,\, q_i)Ce_1'(\xi,\, q_i)\sin\,\omega_i t$$
$$-\,f\beta_1 se_1(\eta,\, q_i)Se_1'(\xi,\, q_i)\cos\,\omega_i t]. \tag{9}$$

The transformation of these modal variables (subscript i) into the layer variables (subscript j) is made by

$$u_j^\xi = \frac{A_{ij}}{\det(a_{ij})}U_i^\xi, \tag{10}$$

$$u_j^\eta = \frac{A_{ij}}{\det(a_{ij})}U_i^\eta, \tag{11}$$

$$\zeta_j = \frac{B_{ij}}{\det(b_{ij})}\pi_i, \tag{12}$$

where u_j^ξ is the radial component of velocity in layer j, u_j^η is the azimuthal component of velocity in layer j, ζ_j is the upper interface displacement of layer j, a_{ij} and b_{ij} are a function of the stratification, and A_{ij} and B_{ij} are the cofactors of a_{ij} and b_{ij}. The upper surface is free, hence $i = 1$ refers to the barotropic solution, $i = 2$ the first vertical mode baroclinic solution, and $i = 3$ the second vertical mode baroclinic solution. The ij are positions within the transformation matrices, defined as in Csanady (1982)

$$a = \begin{bmatrix} -h_2 - h_3 + \varepsilon_{23}\dfrac{h_2 h_3}{D_1} + D_1 & h_2 - \varepsilon_{23}\dfrac{h_2 h_3}{D_1} & h_3 \\[2mm] -h_2 - h_3 + \varepsilon_{23}\dfrac{h_2 h_3}{D_2} + D_2 & h_2 - \varepsilon_{23}\dfrac{h_2 h_3}{D_2} & h_3 \\[2mm] -h_2 - h_3 + \varepsilon_{23}\dfrac{h_2 h_3}{D_3} + D_3 & h_2 - \varepsilon_{23}\dfrac{h_2 h_3}{D_3} & h_3 \end{bmatrix}, \tag{13}$$

$$b = \begin{bmatrix} \dfrac{a_{11}}{h_1} & \dfrac{a_{12}}{h_2} - \dfrac{a_{11}}{h_1} & \dfrac{a_{13}}{h_3} - \dfrac{a_{12}}{h_2} \\[2mm] \dfrac{a_{21}}{h_1} & \dfrac{a_{22}}{h_2} - \dfrac{a_{21}}{h_1} & \dfrac{a_{23}}{h_3} - \dfrac{a_{22}}{h_2} \\[2mm] \dfrac{a_{31}}{h_1} & \dfrac{a_{32}}{h_2} - \dfrac{a_{31}}{h_1} & \dfrac{a_{33}}{h_3} - \dfrac{a_{32}}{h_2} \end{bmatrix}, \tag{14}$$

where

$$\varepsilon_{12} = 1 - \frac{\rho_1}{\rho_2}, \qquad \varepsilon_{23} = 1 - \frac{\rho_2}{\rho_3}, \qquad \varepsilon_{13} = 1 - \frac{\rho_1}{\rho_3}, \tag{15}$$

and

$$D = \begin{cases} H \\ \dfrac{H}{2}[\gamma + (\gamma^2 - 4\delta)^{1/2}] \\ \dfrac{H}{2}[\gamma - (\gamma^2 - 4\delta)^{1/2}] \end{cases}, \tag{16}$$

where H is the total depth, h_j the layer depths, D_i are the equivalent modal depths, and the following definitions are made (Monismith 1985):

$$\gamma = \frac{1}{H^2}(\varepsilon_{12}h_1 h_2 + \varepsilon_{23}h_2 h_3 + \varepsilon_{13}h_1 h_3) \tag{17}$$

$$\delta = \frac{1}{H^3}\varepsilon_{12}\varepsilon_{23}h_1 h_2 h_3 . \tag{18}$$

Circular basin—We can investigate the case in which the aspect ratio goes to unity by looking at the limiting case of a circular basin. The linear solutions for a circular basin of uniform depth are given in Thomson (1879) and Lamb (1932) and the two-layer case is given in Csanady (1967). We present a short description of the solution here for completeness.

We use plane polar coordinates, where r is the radial and θ the angular coordinate. The linear inviscid normal mode equations of motion in a plane polar coordinate system are

$$\frac{\partial U_i^r}{\partial t} - fU_i^\theta = -gD_i\frac{\partial \pi_i}{\partial r}, \tag{19}$$

$$\frac{\partial U_i^\theta}{\partial t} + fU_i^r = -gD_i\frac{\partial \pi_i}{r\partial \theta}. \tag{20}$$

The modal pressure is assumed to be of the form

$$\pi_i = G_i(r)\cos n\theta \cos \omega_i t , \tag{21}$$

with n the azimuthal mode and $G(r)$ the radial structure of the modal pressure. The wave equation becomes

$$\frac{\partial^2 G_i}{\partial r^2} + \frac{1}{r}\frac{\partial G_i}{\partial r} + \left(\frac{\omega_i^2 - f^2}{c_i^2} - \frac{n^2}{r^2}\right)G_i = 0, \tag{22}$$

which for $|\omega_i| > |f|$ represents Bessel's equation and for $|\omega_i| < |f|$ represents the modified Bessel equation. The solution for $G_i(r)$ is

$$G_i(r) = \begin{cases} J_n\left(\dfrac{r}{R_i^*}\right) & |\omega_i| > |f| \\[3mm] I_n\left(\dfrac{r}{R_i^*}\right) & |\omega_i| < |f|, \end{cases} \tag{23}$$

where

$$R_i^* = c_i\big/\sqrt{|\omega_i^2 - f^2|} . \tag{24}$$

Two classes of solution are possible: for superinertial frequencies the solutions are Poincaré waves, because the Bessel function J_n has a periodic form; for subinertial frequencies the solutions are Kelvin waves, because the modified Bessel function I_n has an exponential form. In the discussion to follow, we use the Bessel function J_n everywhere, which is simply replaced by I_n where the Kelvin wave is meant.

The frequency equation for superinertial (Poincaré) waves (Csanady 1967), in which nondimensional variables are used, is
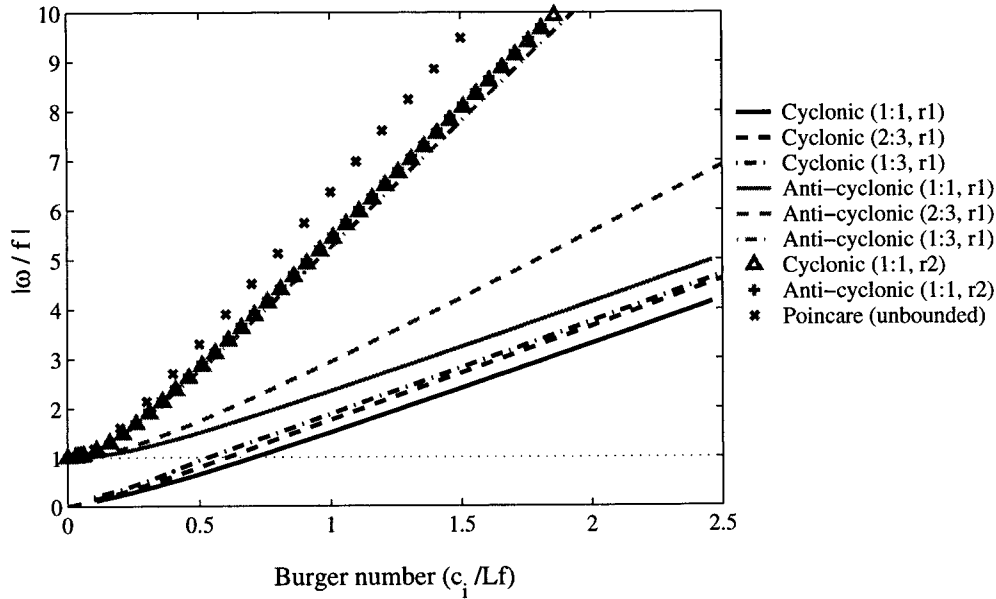
Fig. 1. Nondimensionalized frequency as a function of Burger number $S_i = c_i/Lf$ and wave type: r1, radial mode one; $2:3$, ellipse of aspect ratio $2:3$. All waves are azimuthal mode one, which is equivalent to one sine wave wrapping around lines of constant radius. The length scale L is defined as the wavelength for the unbounded solutions, the basin radius for the circular basin solutions, and the major axis half-length for the elliptic basin solutions. The horizontal dotted line represents the inertial frequency. This figure is valid for all vertical mode waves, because this dependence is captured by c_i in the Burger number.

$$\frac{1}{S_i}\sqrt{\sigma_i^2 - 1}\,J_{n-1}\!\left(\frac{1}{S_i}\sqrt{\sigma_i^2 - 1}\right) + n\!\left(\frac{1}{\sigma_i} - 1\right)J_n\!\left(\frac{1}{S_i}\sqrt{\sigma_i^2 - 1}\right)$$
$$= 0, \qquad (25)$$

where the radius R replaces ϕ in the Burger number (Eq. 5). To determine the frequency equation for subinertial (Kelvin) waves, we replace the Bessel function J by the modified Bessel function I, as in Eq. 23. Solutions can be found to Eq. 25 for all f, R, c_i, and n, whereas subinertial wave solutions are available for a limited subset of n because of the exponential structure of $G(r)$. Lamb (1932, §210) showed that for a subinertial wave solution of azimuthal mode n to exist,

$$S_i < \left[\frac{1}{n(n + 1)}\right]^{1/2}. \qquad (26)$$

Note that the frequency Eq. 25 is an eigenvalue problem, as with the elliptic case (Eq. 7), for which solutions of increasing σ_i correspond to increasing radial mode. The solutions also form pairs, although the frequencies are opposite in sign. The consideration of positive and negative frequencies has allowed us to extend the solutions of Lamb (1932) and Csanady (1967) to superinertial frequencies for cyclonic modes in circular basins. The importance of cyclonic and anticyclonic waves will be made clear in a subsequent section.

The modal transport fields for the circular basin case are

$$U_i^r = \frac{-gD_i}{\omega_i^2 - f^2}\left(\omega_i\frac{dG_i}{dr} + \frac{fn}{r}G_i\right)\sin(n\theta + \omega_i t), \quad (27)$$

$$U_i^\theta = \frac{-gD_i}{\omega_i^2 - f^2}\left(f\frac{dG_i}{dr} + \frac{n\omega_i}{r}G_i\right)\cos(n\theta + \omega_i t), \quad (28)$$

where the transformations are the same as for the elliptic basin. The Bessel functions can be shown to be the limiting case of the Mathieu functions as the aspect ratio becomes unity (McLachlan 1947).

Dispersion relations—The dispersion relation for plane-progressive Poincaré waves in an unbounded system is (Gill 1982)

$$\omega_i^2 = f^2 + c_i^2 k_i^2, \qquad (29)$$

where k_i is the horizontal wavenumber ($2\pi/\lambda$, where λ is the wavelength). A simple expression for the dispersion relation does not exist for circular and elliptic basins of uniform depth, and so we derived the dispersion relations numerically by solving Eqs. 7 and 25 for a range of Burger numbers (Eq. 5). We include only waves of the first azimuthal mode ($n = 1$), the lowest frequency solutions. The length scale L in the Burger number (Eq. 5) was taken as the wavelength $\lambda = 2\pi/\sqrt{k_i^2 + l_i^2}$ for the unbounded case, the radius R for the circular basin, and the major axis half-width ϕ for the elliptic basin. The results are presented in Fig. 1. The coefficients of polynomials fitted to the dispersion relations are presented in Table 1.

Table 1. Polynomial coefficients for curves fitted to the dispersion relations in Fig. 1. The fitted polynomial takes the form $\omega/f = a_0 + a_1 S + a_2 S^2 + a_3 S^3$. For the unbounded case, $\omega/f = \sqrt{1 + 4\pi^2 S^2}$. For radial mode 2, the curves are shown for anticyclonic waves only. The nondimensional frequencies for cyclonic waves are <2% lower for radial mode 2 and <1% lower for radial mode 3.

Wave, radial mode	Aspect	S range	a_0	a_1	a_2	a_3
Cyclonic						
1	1:1	0–0.5	0.00	1.01	0.615	—
1	1:1	0.5–2.5	−0.279	1.79	—	—
Anticyclonic						
1	1:1	0–0.5	1.00	0.015	2.97	−1.95
1	1:1	0.5–2.5	0.565	1.79	—	—
2	1:1	0–0.5	1.00	0.377	11.9	−10.4
2	1:1	0.5–2.5	0.189	5.28	—	—
Cyclonic						
1	2:3	0–0.5	0.00	1.22	0.761	—
1	2:3	0.5–25	−0.147	1.90	—	—
Anticyclonic						
1	2:3	0–0.5	1.00	0.009	4.67	−0.346
1	2:3	0.5–2.5	0.359	2.60	—	—
Cyclonic						
1	1:3	0–0.5	0.00	1.57	0.587	—
1	1:3	0.5–2.5	0.002	1.88	—	—
Anticyclonic						
1	1:3	0–0.5	1.00	0.303	11.1	−9.34
1	1:3	0.5–2.5	0.171	5.09	—	—

For the anticyclonic Poincaré waves, the frequency remains superinertial in all cases, with frequency decreasing to the inertial frequency as the Burger number decreases to 0. This is equivalent to the basin dimension becoming infinite, such as in the ocean, which results in the observation of inertial motion. For the cyclonic Poincaré waves, a similar pattern is observed, except for the radial mode one wave, which becomes subinertial at low Burger number. This wave changes its spatial character (see subsequent section below) as the Burger number decreases to 0, becoming what is known as a Kelvin wave. It is clear that the radial mode one waves exhibit substantially different characteristics to the higher radial mode waves. For higher radial modes, the frequencies of the cyclonic and anticyclonic waves differ only slightly. The small (<2%) difference in the frequencies means that higher radial modes are most likely to be observed as standing waves in a rotating system, with the cyclonic and anticyclonic waves traveling in opposite directions with almost the exact frequency. The large difference in frequency between the cyclonic and anticyclonic waves of radial mode one results in the observation of waves of increasingly diverging frequency for decreasing Burger number.

For zero rotation in the case of an elliptic basin, two solutions are possible. Both solutions are standing waves; one oriented longitudinally, and the other oriented transversely. The longitudinal standing mode is described by the terms containing α_n in Eq. 6 and the transverse standing modes by the terms containing β_n. As the effect of rotation increases (the Burger number decreases), the α_n and β_n become of increasingly similar magnitude, and the modes rotate. The longitudinal mode becomes the cyclonic mode, and the transverse mode becomes the anticyclonic mode.

For zero rotation in a circular basin and $n \geq 1$, the cyclonic and anticyclonic modes combine to form the fundamental standing wave. As the rotation increases (the Burger number decreases), the frequencies begin to increasingly diverge for the lowest radial mode, and standing waves are no longer possible. As the Burger number decreases below $1/\sqrt{2}$ (see Eq. 26) for azimuthal mode one, the cyclonic mode becomes increasingly like a Kelvin wave. The radial properties of the lowest radial modes are explained further in a subsequent section.

Note that the vertical mode has no effect on the dispersion relation, because its dynamical effect is incorporated entirely into the nonrotating phase speed c_i in the Burger number (Eq. 5).

Energy partitioning

Basin total—The energy ratio for unbounded waves in a rotating system is given by Eq. 1. For the circular and elliptic basins, the energy was integrated over the whole basin volume and averaged over one period. The total potential energy equation for a wave disturbance in a circular basin is

$$\mathrm{PE}_{\mathrm{wave(total)}} = \frac{g}{2} \int_0^{2\pi} \int_0^R [(\rho_3 - \rho_2)(\zeta_3^2 + \zeta_3 h_3)$$
$$+ (\rho_2 - \rho_1)(\zeta_2^2 + 2\zeta_2 h_2 + 2\zeta_2 h_3)$$
$$+ \rho_1(\zeta_1^2 + 2\zeta_1 H)]r \, dr \, d\theta \qquad (30)$$

and the total kinetic energy equation is

$$\mathrm{KE}_{\mathrm{wave(total)}} = \frac{1}{2} \int_0^{2\pi} \int_0^R [\rho_3(h_3 + \zeta_3)(u_{r_3}^2 + u_{\theta_3}^2)$$
$$+ \rho_2(h_2 + \zeta_2 - \zeta_3)(u_{r_2}^2 + u_{\theta_2}^2)$$
$$+ \rho_1(h_1 + \zeta_1 - \zeta_2)(u_{r_1}^2 + u_{\theta_1}^2)]r \, dr \, d\theta$$
$$(31)$$

where the subscripts refer to the layer index (numbered from the surface). For elliptic basins, the integral bound R is replaced by ξ_0, and $rdrd\theta$ is replaced by $0.5(\phi^2 - \psi^2)(\cosh 2\xi - \cos 2\eta)d\xi d\eta$. The ratio of potential to kinetic energy for linear, long internal gravity waves in rotating, circular, and elliptic lakes are presented in Fig. 2. The coefficients of polynomials fitted to the energy ratios are presented in Table 2.

The solutions are linear and so are independent of the amplitude of the waves. The ratio of total potential to total kinetic energy is dependent only on the density structure $\rho(z)$ through c_i—that is, two different density structures that result in the same value of c_i will have the same ratio of total potential to total kinetic energy. The nature of the stratification is entirely contained within the nonrotating phase speed c_i, as with the dispersion relation (Fig. 1). That is,
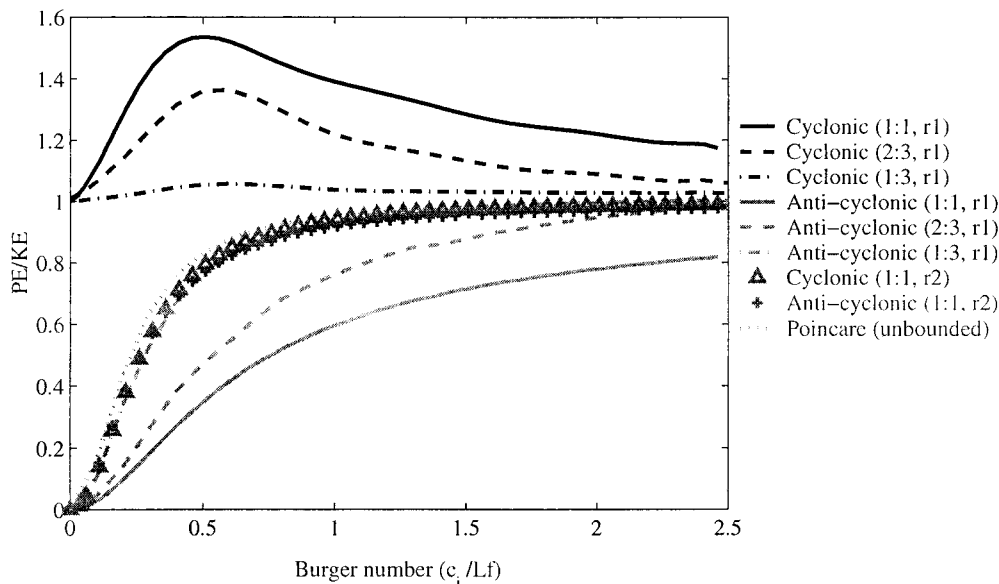
Fig. 2. Ratio of total potential to kinetic energy, integrated over the volume and averaged over one period, as a function of Burger number $S_i = c_i/Lf$. The length scale L is defined as in Fig. 1. This figure is valid for all vertical mode waves, because this dependence is captured by c_i in the Burger number.

$$\frac{\text{PE}_{\text{total}}}{\text{KE}_{\text{total}}} = f\left(S_i, \frac{\psi}{\phi}, m, n\right), \qquad (32)$$

where m is the radial mode. Note that the ratio is independent of the vertical mode, because this is accounted for through the nonrotating phase speed c_i in the Burger number.

For the cyclonic, lowest radial mode, the ratio is at all times greater than unity. The ratio for a rectilinear Kelvin wave propagating in a channel is unity (Gill 1982), which the solution approaches as the Burger number approaches 0. The transition at the inertial frequency ($S_i = 1/\sqrt{2}$ for a circular basin) sees no appreciable change in the energy partitioning. As the Burger number increases, the ratios for the lowest radial mode waves slowly converge to unity.

The energy partitioning in anticyclonic basin-scale waves favors kinetic energy. This is also the case for cyclonic waves other than radial mode one. The trend becomes stronger for low Burger numbers, which equate to large, weakly stratified, strongly rotating systems. This is equivalent to the unbounded case of plane progressive Poincaré waves. For nonrotating systems, as S_i becomes infinite, the ratio approaches unity. As the Burger number increases, gravity plays a more important role in wave dynamics, and as the Burger number decreases rotation becomes more important. Burger numbers for several lakes are presented in Table 3. An important feature to note is that, for a particular lake, the Burger number will change with season as the stratification increases and decreases through the nonrotating phase speed c_i. The energy partitioning within the same mode, in the same lake, will thus change depending on when the system is sampled.

The effect of decreasing the aspect ratio on energy partitioning is to move toward the nonrotating case, especially for the cyclonic waves. This is due to the "effective" Burger number (averaged around the basin perimeter) decreasing with decreasing aspect ratio. The circular basin case can therefore be considered to represent the maximum and minimum possible ratios of potential to kinetic energy.

Radial structure—Potential and kinetic energy at a point, integrated over depth, has the following functional dependence

$$PE, KE = f[S, m, n, vm, A, \rho(z), r, \theta], \qquad (33)$$

where r is the local radial coordinate, θ the local azimuthal coordinate, vm the vertical mode, and A the amplitude. Both the PE and KE values oscillate with time, but we are interested in only the mean values in this case. We consider only the circular basin case to simplify the discussion and present the radial structure of these values, nondimensionalized by their maximum, as a function of the nondimensional radius r/R in Fig. 3 for the vertical mode 1, azimuthal mode 1, radial mode 1 (v1, a1, and r1), and cyclonic and (v1, a1, and r1) anticyclonic waves. The structure for higher vertical modes is the same as the first vertical mode. The extension of the radial structure to the elliptic basin is made by defining the length scale in the Burger number (Eq. 5) as half the basin width along the line of constant η that is of interest. For example, a lake where $c = 0.33$ m s^{-1}, $f = 7.81 \times 10^{-5}$ rad s^{-1}, $\phi = 7,500$ m, and $\psi = 5,000$ m gives a Burger number of 0.56 if considering the radial structure along major axis and a Burger number of 0.85 if considering the radial structure along the minor axis.

For the anticyclonic (Poincaré) waves (Fig. 3b,d), the KE is largest at the lake center. The PE is largest approaching the boundary, as shown by Csanady (1967). As the Burger number increases (the effect of rotation decreases), the PE becomes largest at the shore, as in a nonrotating seiche. The

Table 2. Polynomial coefficients for curves fitted to the energy ratios in Fig. 2. The fitted polynomial takes the form $PE/KE = a_0 + a_1S + a_2S^2 + a_3S^3 + a_4S^4$. For the unbounded case, $PE/KE = 2\pi^2S^2/(2\pi^2S^2 + 1)$. For radial mode 2, the curves are shown for anticyclonic waves only. The energy ratios for cyclonic waves are <2% lower for radial mode 2 and <1% lower for radial mode 3.

Wave, radial mode	Aspect	S range	a_0	a_1	a_2	a_3	a_4
Cyclonic							
1	1:1	0–0.5	1.0	0.954	3.42	−6.34	—
1	1:1	0.5–2.5	1.73	−0.407	0.075	—	—
Anticyclonic							
1	1:1	0–0.5	0.0	0.059	2.68	−2.83	—
1	1:1	0.5–2.5	−0.043	1.00	−0.431	0.068	—
2	1:1	0–0.5	0.0	0.211	14.8	−41.0	33.4
2	1:1	0.5–2.5	0.537	0.665	−0.347	0.061	—
Cyclonic							
1	2:3	0–0.5	1.0	0.459	1.78	−2.40	—
1	2:3	0.5–2.5	1.57	−0.430	0.092	—	—
Anticyclonic							
1	2:3	0–0.5	0.0	0.092	4.03	−4.66	—
1	2:3	0.5–2.5	−0.024	1.28	−0.596	0.099	—
Cyclonic							
1	1:3	0–0.5	1.0	0.082	0.076	—	—
1	1:3	0.5–2.5	1.08	−0.054	0.013	—	—
Anticyclonic							
1	1:3	0–0.5	0.0	1.27	3.32	−5.62	—
1	1:3	0.5–2.5	0.458	0.854	−0.457	0.081	—

shapes are independent of the vertical mode. For low Burger number, the radial mode one cyclonic wave field (Fig. 3a,c) shows the exponential structure of linear Kelvin waves propagating along a single infinite vertical boundary (Gill 1982). As the Burger number increases, the potential energy structure becomes less exponential, being almost linear at $S \approx 0.8$ and approaching the anticyclonic radial structure as the Burger number continues to increase. The transition between the Kelvin wave feature of kinetic energy concentration at the shoreline and Poincaré wave feature of kinetic energy concentration in the lake interior occurs around $S = 1.0$ (Fig. 3c). At $S = 4.0$—that is, when the internal Rossby radius is twice the basin diameter—the radial structures of the solutions have almost converged. At this Burger number, the PE/KE ratio is 1.11 and 0.89 for the cyclonic and anticyclonic

waves, respectively. The nondimensional frequencies for these waves are 6.97 and 7.8, respectively. The difference in ratios does not decrease to <5% until $S \approx 8$, when the internal Rossby radius is four times the basin diameter.

The extension of the circular basin solution of Lamb (1932) and Csanady (1967) to superinertial frequencies for cyclonic waves allows us to describe the formation of Kelvin and Poincaré waves from a simple standing wave in a nonrotating system. A standing wave is well-known to be made up of two progressive waves traveling in opposite directions (Turner 1973). A standing wave in a circular basin for zero rotation (i.e. infinite Burger number) will thus be made up of two progressive waves with identical potential and kinetic energy signatures (as in Fig. 3 for high S). As the rotation increases (the Burger number decreases), the lowest radial

Table 3. Burger numbers (c_i/Lf) for several lakes. Mono Lake, Lake Maracaibo, and Lake Taupo can be considered circular; Lake Kinneret, Biwa, Michigan, and Ontario ellipses of aspect ratio 2/3, 1/2, 1/3, and 1/4, respectively. L represents the basin radius for a circular basin and the major axis half-length for an ellipse. vm = vertical mode.

| Lake	vm	c (ms^{-1})	L (m)	f (rad s^{-1})	S	Source
Mono (USA)	1	0.74	4,000	8.95e−5	2.07	MacIntyre et al. (1999)
	2	0.22	4,000	8.95e−5	0.61	
Kinneret (Israel)	1	0.33	7,500	7.81e−5	0.56	Antenucci et al. (2000)
	2	0.16	7,500	7.81e−5	0.27	
Biwa (Japan)	1	0.45	15,000	8.17e−5	0.37	Saggio and Imberger (1998)
Maracaibo (Venezuela)	1	0.44	55,000	2.53e−5	0.32	de Bautista (1997)
Taupo (New Zealand)	1	0.11	10,000	9.14e−5	0.12	Gilmour and Heath (1989)
Ontario (Canada)	1	0.5	120,000	1e−4	0.04	Csanady (1973)
Michigan (USA)	1	0.48	160,000	1e−4	0.03	Csanady (1973)
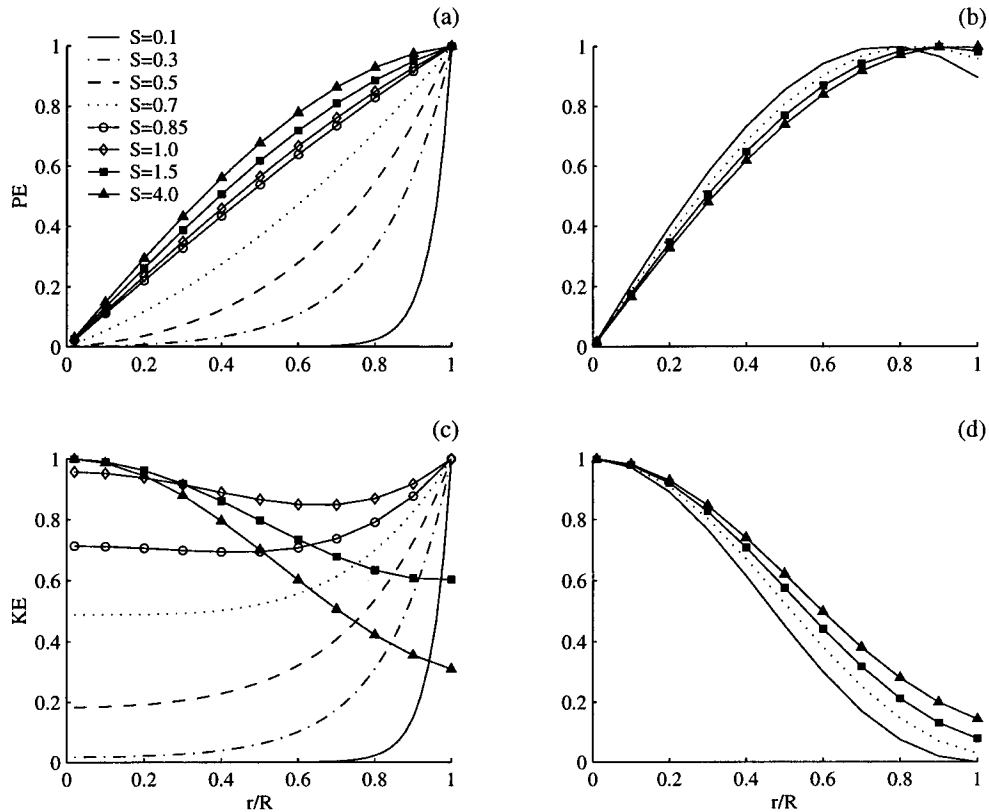
Fig. 3. Radial structure of cyclonic and anticyclonic radial mode one wave energy distribution as a function of Burger number. The cyclonic wave structure is shown in panels (a) and (c). The anticyclonic wave structure is shown in panels (b) and (d). The radial structure for each Burger number has been normalized by its maximum value. Note that not all Burger numbers are shown in panels (b) and (d).

cyclonic mode changes character, becoming increasingly exponential (a ''Kelvin'' wave), whereas the anticyclonic mode undergoes only minor changes.

Experimental application

The motivation for this work was to determine the dissipation timescale for basin-scale waves in a rotating system. The first problem was to determine the total amount of energy in a basin-scale wave in a rotating system, which the above analysis aims to do. Once this is determined, a dissipation timescale may be found by estimating an appropri-

ate rate of dissipation. Another application of the model is in estimating isopycnal displacements and velocity scales in regions not sampled by use of a single measurement of potential energy fluctuations.

The field site that motivated this work is Lake Kinneret, Israel. Field measurements of temperature and velocity fluctuations by Antenucci et al. (2000) were characteristic of a basin-scale internal wave field that could be described by a three-layer, circular basin model. The basin-scale internal waves found in Lake Kinneret are summarized in Table 4.

The objective of the experimental application was to use both the circular and elliptic basin models to determine the total amount of energy in basin-scale internal waves in Lake Kinneret by use of a single point measurement of potential energy fluctuations (in this case, a thermistor chain). This has not previously been possible for waves in enclosed, rotating systems. We then show how a dissipation timescale of the basin-scale internal waves may be derived. We also demonstrate how approximate values for isopycnal displacements and velocity scales may be determined from the point measurement of potential energy fluctuations. Limitations of the experimental application are then discussed.

We chose to use a two-layer approximation to the stratification, because we were interested in this case in only the vertical mode one waves. A surface layer of 11 m thickness

Table 4. Basin-scale internal waves found in Lake Kinneret by Antenucci et al. (2000).

Period (h)				
Field	Three-layer model	Vertical mode	Horizontal mode	Wave type
24	22.5	One	One	Cyclonic (Kelvin)
12	12.2	One	One	Anticyclonic (Poincaré)
20 ± 2	17.5	Two	One	Anticyclonic (Poincaré)
20 ± 2	—	Three	One	Anticyclonic (Poincaré)

and 28°C and a lower layer of 13 m thickness and 20°C was used, as in Antenucci et al. (2000). To determine the amplitude of the displacement of the two-layer interface required to match the potential energy fluctuations measured at each frequency, Antenucci et al. (2000) used continuous wavelet transforms of the potential energy signal, derived from thermistor chain measurements. Typical amplitudes at the measurement station (Fig. 4; for an elliptic basin, $\xi = 0.2067$ and $\eta = 1.212$; for a circular basin, $r/R = 0.25$) were found to be 1.5 m for the Kelvin wave and 0.7 m for the Poincaré wave. Alternatively, an estimate of the interface deflection could be made via inspection of the thermistor chain records.

We scaled both the elliptic and circular basin solution on the basis of this observation. For a two-layer system, the transformation matrices (13–16) are

$$a = \begin{bmatrix} h_1 - \varepsilon_{12}\dfrac{h_1 h_2}{D_1} & h_2 \\[2ex] h_1 - \varepsilon_{12}\dfrac{h_1 h_2}{D_2} & h_2 \end{bmatrix}, \qquad b = \begin{bmatrix} \dfrac{a_{11}}{h_1} & \dfrac{a_{12}}{h_2} - \dfrac{a_{11}}{h_1} \\[2ex] \dfrac{a_{21}}{h_1} & \dfrac{a_{22}}{h_2} - \dfrac{a_{21}}{h_1} \end{bmatrix},$$

$$D = \begin{bmatrix} h_1 + h_2 \\[2ex] \varepsilon_{12}\dfrac{h_1 h_2}{h_1 + h_2} \end{bmatrix}, \qquad \varepsilon_{12} = 1 - \frac{\rho_1}{\rho_2}. \qquad (34)$$

When these relations are used, the equation for the maximum displacement of the internal interface due to the vertical mode one wave is

$$\zeta_2^{\max}(r, \theta) = \frac{h_1(H - \varepsilon_{12}h_2)}{H^2 - \varepsilon_{12}h_1 h_2} A\pi_i^{\max}, \qquad (35)$$

where $\pi_i^{\max}$ is the maximum value of the modal pressure during a period, the appropriate form for π_i is substituted for either the circular or elliptic basin, and (r, θ) is replaced by (ξ, η) in the elliptic basin. The length scale chosen for the circular approximation was 6,200 m and was 7,500 m for the elliptic approximation, giving Burger numbers of 0.68 and 0.56, respectively. For our station location, the value for ζ_2 was determined earlier from observation, leaving the scaling parameter A as the only unknown. This was computed to be 123.6 and 5.97 for the Kelvin and Poincaré wave, respectively, for the circular basin and 82.1 and 99.8 for the elliptic basin. We are now in a position to compute the total potential energy in the vertical mode one Kelvin and Poincaré waves.

The total potential energy equation for a two-layer system, as distinct from the three-layer case (Eq. 30), is

$$PE_{\text{wave(total)}} = \frac{g}{2} \int_0^{2\pi} \int_0^R [(\rho_2 - \rho_1)(\zeta_2^2 + 2\zeta_2 h_2)$$
$$+ \rho_1(\zeta_1^2 + 2\zeta_1 h_1 + 2\zeta_1 h_2)]r\, dr\, d\theta, \qquad (36)$$

where ζ_2 for the internal mode is as above and ζ_1, the surface deflection due to the internal wave, is
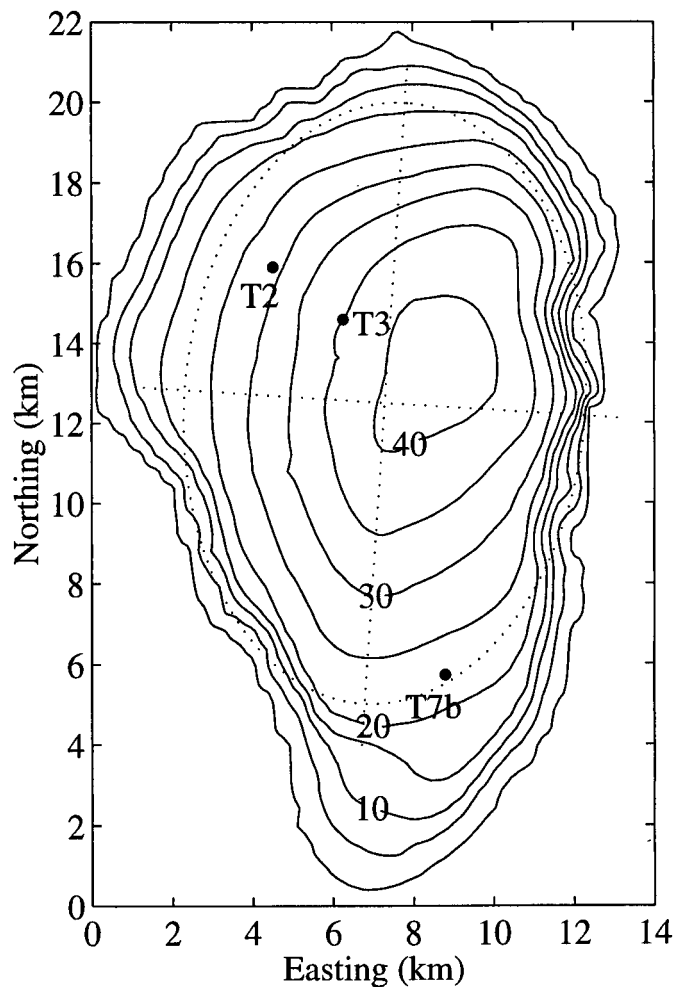

Fig. 4. Lake Kinneret bathymetry with location of thermistor chains. Sta. T2 and T3 are aligned along the primary wind axis. An ellipse of aspect ratio $2:3$ (10,000:15,000 m) is superimposed for use in the discussion. The origin of the map grid is situated at 35.51°N and 32.70°E.

$$\zeta_1(r) = -\frac{\varepsilon_{12}h_1 h_2}{H^2 - \varepsilon_{12}h_1 h_2} A\pi_i = -\frac{\varepsilon_{12}h_2}{H - \varepsilon_{12}h_2}\zeta_2(r)$$

$$\approx -\frac{\varepsilon_{12}h_2}{H}\zeta_2(r). \qquad (37)$$

For the circular basin case, the total PE in the waves was computed to be 1.13×10^{10} and 1.15×10^9 J for the Kelvin and Poincaré wave, respectively. When the total ratios determined from Fig. 2 and Table 2 are used on the basis of the Burger number, this gives a total energy of the Kelvin wave as 1.89×10^{10} J and the total energy of the Poincaré wave as 3.65×10^9 J during the summer (June/July) of 1998. For the elliptic basin, the average total PE was computed to be 2.22×10^{10} and 6.58×10^8 J, giving the total energy of the Kelvin wave as 3.85×10^{10} J and the total energy of the Poincaré wave as 1.92×10^9 J.

Previous investigators have postulated that basin-scale waves are dissipated primarily in the benthic boundary layer (Imberger 1998; Saggio and Imberger 1998). To estimate a
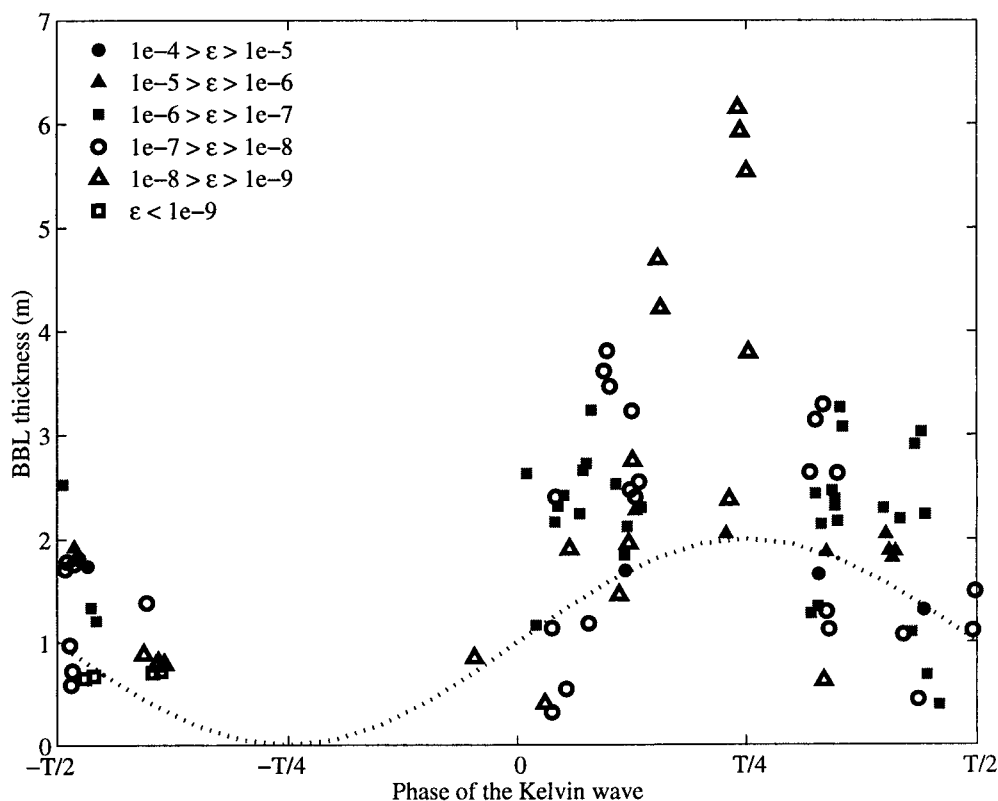
Fig. 5. Benthic boundary layer thickness (accurate to ±0.1 m) and rate of dissipation of turbulent kinetic energy as a function of the phase of the basin-scale Kelvin wave at Sta. T2 (22 m). Phase was determined via a continuous wavelet transform of the vertically integrated potential energy signal derived from a thermistor chain. Boundary layer properties were determined via analysis of temperature microstructure profiles. The dotted sine curve is shown to demonstrate the phase of the wave.

timescale for the dissipation of these waves, we used results from extensive temperature microstructure profiles to determine the rate of dissipation of turbulent kinetic energy in the benthic boundary layer using Batchelor fitting (Luketina and Imberger 2001). From thermistor chain data, we determined the phase of the Kelvin wave using continuous wavelet transforms of the integrated potential energy signal (Antenucci et al. 2000). The depth of the benthic boundary layer, along with the dissipation, is plotted against the phase of the Kelvin wave in Fig. 5 for the 99 profiles available at Sta. T2 (Fig. 4). The benthic boundary layer was defined as the region near the bottom where the density was constant and the turbulence was statistically stationary. Data were segmented into statistically stationary components by use of the method of Imberger and Ivey (1991). The ensemble average energy dissipation over one cycle of the Kelvin wave may be calculated from

$$D = \sum_{i=1}^{99} \rho \varepsilon_i h_i \Delta t_i, \qquad (38)$$

where ε_i is the dissipation in the benthic boundary layer for profile i (m^2 s^{-3}), h_i the boundary layer thickness (m), ρ the density (kg m^{-3}), and Δt_i the time between profiles (s). Evaluation of Eq. 38 gives 132 J m^{-2} cycle^{-1}. To determine the dissipation of the Kelvin wave (the most energetic wave),

we first defined the total energy as $E = 0.5\rho U^2 V$, where U is a velocity scale and V the lake volume. Defining $\varepsilon = \kappa U^3 / h$ and $dI/dt = -AD/T$, where T is the Kelvin wave period and A is the area intersected by the metalimnion (3.4×10^7 m^2), it can be shown that

$$\frac{E}{E_0} = \frac{1}{(1 + t/t_D)^2}, \qquad (39)$$

where $t_D = 2E_0 T/AD$. Substituting the above values gives $t_D = 8.5$ d for the circular basin, which results in 3.5 d for the Kelvin wave to decay to one half of its initial energy. This increases to 7 d for the elliptic basin, because of the increased estimate of the Kelvin wave energy. Note that this assumes that the benthic boundary layer dissipation measured at one station, averaged over a wave period, is representative of a basin-wide average. Future efforts will focus on obtaining measurements to get an improved basinwide average, particularly in the radial direction, from which a more accurate decay timescale can be determined.

The scales of isopycnal displacement and velocity are presented in Fig. 6 for an elliptic approximation to Lake Kinneret, as discussed above. The cyclonic mode (a Kelvin wave) has the largest velocities near the boundaries, whereas the anticyclonic mode (a Poincaré wave) has largest velocities in the interior. The fields have been scaled by the mea-
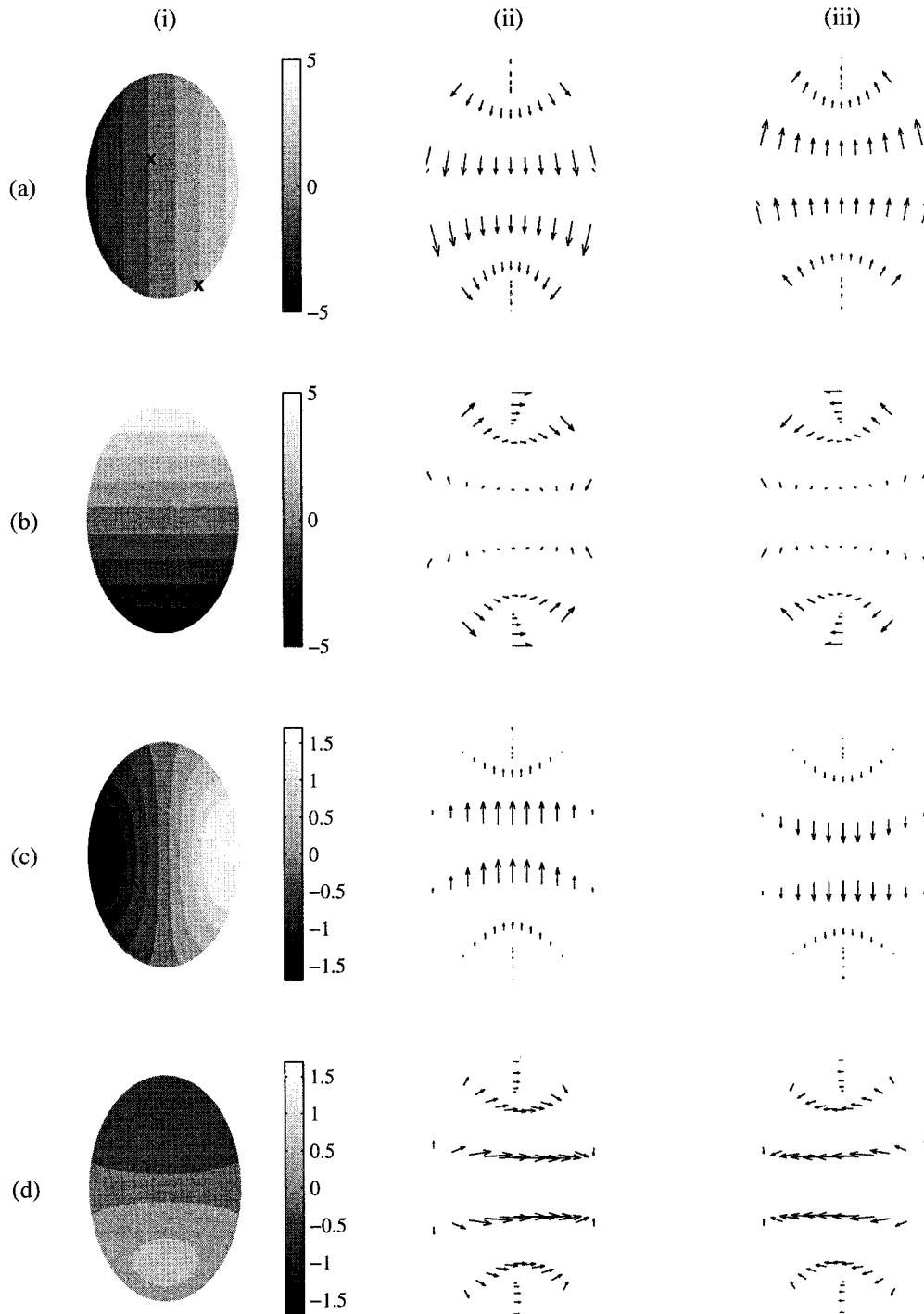
Fig. 6. Dynamical fields for a uniform-depth elliptical basin (major axis 15,000 m, minor axis 10,000 m) situated at 32.5°N for a two-layer approximation. The vertical mode one, azimuthal and radial mode one Kelvin wave solution is shown in (a) and (b), for two times separated by T/4; the vertical mode one, azimuthal, and radial mode one Poincaré wave solution in (c) and (d). Column (1) shows the displacement of the internal interface in m; (2) velocity vectors in the upper layer; and (3) velocity vectors in the lower layer. Velocity vectors are normalized by the maximum velocity for each wave, shown in Table 5. The crosses in (a and 1) show the approximate location of Sta. T3 and T7b from Fig. 4.

Table 5. Basin-wide maximum amplitude of the internal interface and maximum layer speeds in a two-layer elliptic approximation to Lake Kinneret, as a function of phase.

Wave	T	ζ_2^{max} (m)	U_1^{max} (m s^{-1})	U_2^{max} (m s^{-1})
Cyclonic	0	3.4	0.14	0.12
Cyclonic	T/4	5.0	0.07	0.06
Anticyclonic	0	1.7	0.04	0.03
Anticyclonic	T/4	0.68	0.06	0.05

Table 6. Maximum amplitude of the internal interface and maximum layer speeds in a two-layer elliptic approximation to Lake Kinneret at two measurement locations. Amplitudes in boldface type were observations used to scale the solutions.

Wave	Station	ζ_2^{max} (m)	U_1^{max} (m s^{-1})	U_2^{max} (m s^{-1})
Cyclonic	T3	**1.5**	0.08	0.07
Cyclonic	T7	4.6	0.08	0.07
Anticyclonic	T3	**0.7**	0.06	0.05
Anticyclonic	T7	0.69	0.02	0.01

sured values at Sta. T3, the approximate position of which is shown in the figure. The maximum amplitude and velocities for the waves corresponding to the figure are presented in Table 5. Note that the maximum Kelvin wave amplitudes occur when the crest and trough are in the ellipse cusp, whereas for the Poincaré wave the maximum amplitudes occur when the crest and trough are along the long ellipse side. For maximum velocities, the pattern is reversed.

Field measurements of isotherm displacement were also available during this time from Sta. T7b (Fig. 4), the approximate position of which is shown in Fig. 6. From the two-layer ellipse model, scaled by our observations at Sta.

T3, we calculated the maximum amplitudes and velocities of both the Kelvin and Poincaré waves at this station. These are presented in Table 6. Note that, for the cyclonic wave, the velocity scales are similar at both stations, although the amplitude at Sta. T7 is three times that at Sta. T3. For the anticyclonic wave, the amplitudes at both stations are similar, although the velocities at Sta. T3 are several times greater than those at Sta. T7.

The isotherm displacement record at Sta. T3 and T7b is shown in Fig. 7. The crests of the 24-h Kelvin wave and the 12-h Poincaré wave are shown in Fig. 7b, and the predicted
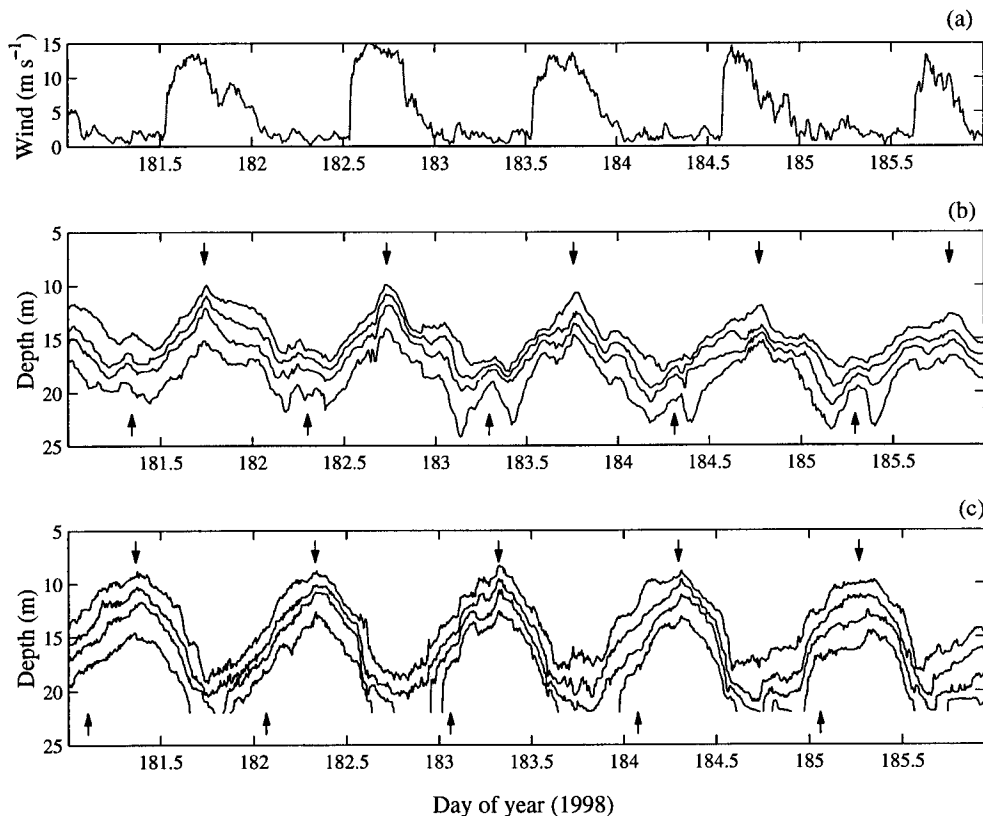

Day of year (1998)

Fig. 7. Field data collected at Lake Kinneret. The wind speed at Sta. T3 (corrected to 10 m elevation) is shown in (a), and isotherm displacements at Sta. T3 and T7b are shown in (b) and (c). Only the metalimnion is shown, with the contour interval 2°C and the top isotherm 24°C. Downward-pointing arrows in (b) show the crests of the 24-h Kelvin wave, and upward-pointing arrows the crests of the 12-h Poincaré wave (where every second Poincaré crest has been omitted), determined from observation at Sta. T3. Downward-pointing arrows in (c) show the computed arrival time of the Kelvin wave at Sta. T7b and upward-pointing arrows the computed arrival time of the Poincaré wave, based on the arrows in (b).

arrival times of both waves at Sta. T7b are shown in Fig. 7c. The field measurements show the increased amplitude of the Kelvin wave, predicted by the linear elliptic basin model as shown in Fig. 6 and Table 5. The difference in amplitude of the Kelvin wave can not be entirely attributed to the characteristics of the waves in the elliptic basin model, because of the absence of a sloping bottom or nonlinear effects in the model. The Poincaré wave signal is not apparent in the record at Sta. T7b, although the model predicts the amplitude should be similar to that at Sta. T3. Clearly, the ellipse model, although it gives a general picture of the effect of the lateral boundary on wave amplitudes, does not capture the localized features of the waves, particularly effects induced by the bottom boundary.

Discussion

The analytical model presented above makes both the linear and long-wave approximations, and so some care is required in its application. The theory does not take into account the nonlinear steepening of basin-scale modes into packets of solitary waves (Thorpe et al. 1972; Farmer 1978; Grimshaw 1998), nor the resonant generation of linear Poincaré waves by nonlinear Kelvin waves (Melville et al. 1989). The model is thus only strictly valid for small amplitude waves, for times less than the steepening timescale T_S (Horn et al. 2001) after the generation of the wave. The steepening timescale T_S for Lake Kinneret is >40 h, greater than the return period of the daily wind forcing, so steepening of the basin-scale waves into solitary waves can be neglected in the experimental application presented above. The only effects of topography included in the model are simple variations in the lateral boundary, and so the model must only be considered a first approximation to systems in which the effect of the bottom boundary or complex lateral boundaries is expected to be strong.

An important aspect of the model presented is the appearance of the nonrotating phase speed c_i in the Burger number. This implies that the characteristics of the basin-scale waves can change dramatically with season. During the unstratified period, c_i will be effectively 0. The Burger number will also be effectively 0, and therefore inertial waves will dominate the system. As the lake heats, the Burger number increases (as c_i increases), and Kelvin and Poincaré waves are possible. During late summer, the lake will reach a maximum stratification—that is, a seasonal peak in the Burger number—at which time the basin-scale waves will be the closest to gravity waves. As the lake cools, the Burger number will decrease, and any basin-scale internal waves present will become increasingly dominated by the earth's rotation.

Dispersion relations and ratios of total potential to kinetic energy have been derived for a rotating, enclosed basin, equivalent to a lake affected by the earth's rotation. The dispersion relation and total energy ratio are dependent only on the direction of relative rotation, azimuthal mode n, radial mode m, the aspect ratio ψ/ϕ, and the Burger number c_i/Lf. Information regarding the structure of the stratification and the vertical mode were found to be entirely captured by the nonrotating phase speed c_i.

Total potential to kinetic energy ratios are substantially less than unity for the anticyclonic (Poincaré waves as $\omega > f$) waves. For the cyclonic, radial mode one waves (a Kelvin wave if $\omega < f$, otherwise a Poincaré wave), the ratio is greater than unity. The anticyclonic waves (and all cyclonic waves other than radial mode one) may be described by a simple rotation/gravity balance captured by the Burger number. For high Burger numbers, gravity dominates, and the waves have an equal partitioning between potential and kinetic energy. For low Burger numbers, rotation dominates and the majority of energy is kinetic. This is the same balance as for unbounded waves in the ocean.

References

ANTENUCCI, J. P., J. IMBERGER, AND A. SAGGIO. 2000. Seasonal evolution of the basin-scale internal wave field in a large stratified lake. Limnol. Oceanogr. **45:** 1621–1638.

CSANADY, G. T. 1967. Large-scale motion in the Great Lakes. J. Geophys. Res. **72:** 4151–4162.

———. 1973. Transverse internal seiches in large oblong lakes and marginal seas. J. Phys. Oceanogr. **3:** 439–447.

———. 1975. Hydrodynamics of large lakes. Annu. Rev. Fluid Mech. **7:** 357–386.

———. 1982. On the structure of transient upwelling events. J. Phys. Oceanogr. **12:** 84–96.

CUSHMAN-ROISIN, B. 1994. Introduction to geophysical fluid dynamics. Prentice Hall.

DE BAUTISTA, S. H. 1997. Proceso de Salinizacion en el Lago de Maracaibo. ICLAM.

FARMER, D. M. 1978. Observations of long nonlinear internal waves in a lake. J. Phys. Oceanogr. **8:** 63–73.

GILL, A. E. 1982. Atmosphere-ocean dynamics. Academic.

GILMOUR, A. E., AND R. A. HEATH. 1989. Barotropic and baroclinic waves in Lake Taupo. N. Z. J. Mar. Freshw. Res. **23:** 189–194.

GOLDSTEIN, S. 1929. Tidal motion in rotating elliptic basins of constant depth. Monthly Notices R. Astron. Soc. (Geophys. Supp.). **2:** 213–231.

GRIMSHAW, R. 1998. Internal solitary waves in shallow seas and lakes, p. 227–239. *In* J. Imberger [ed.], Physical processes in lakes and oceans. AGU.

HORN, D. A., J. IMBERGER, AND G. N. IVEY. 2001. The degeneration of large-scale interfacial gravity waves in lakes. J. Fluid Mech. **434:** 181–207.

IMBERGER, J. 1994. Transport processes in lakes: A review, p. 99–193. *In* R. Margalef [ed.], Limnology now: A paradigm of planetary problems. Elsevier.

———. 1998. Flux paths in a stratified lake, p. 1–17. *In* J. Imberger [ed.], Physical processes in lakes and oceans. AGU.

———, AND G. N. IVEY. 1991. On the nature of turbulence in a stratified fluid—part 2: Application to lakes. J. Phys. Oceanogr. **21:** 659–680.

JEFFREYS, H. 1925. The free oscillations of water in an elliptical lake. Proc. Lond. Math. Soc. **23:** 455–476.

LAMB, SIR H. 1932. Hydrodynamics, 6th ed. Dover.

LUKETINA, D. A., AND J. IMBERGER. 2001. Determining turbulent kinetic energy dissipation from Batchelor curve fitting. J. Atmos. Ocean. Tech. **18:** 100–113.

MACINTYRE, S., K. M. FLYNN, R. JELLISON, AND J. R. ROMERO. 1999. Boundary mixing and nutrient fluxes in Mono Lake, California. Limnol. Oceanogr. **44:** 512–529.

MCLACHLAN, N. W. 1947. Theory and application of Mathieu functions. Oxford Univ. Press.

MELVILLE, W. K., G. G. TOMASSON, AND D. P. RENOUARD. 1989. On the stability of Kelvin waves. J. Fluid Mech. **206:** 1–23.

MONISMITH, S. G. 1985. Wind-forced motions in stratified lakes and their effect on mixed-layer shear. Limnol. Oceanogr. **30:** 771–783.

MORTIMER, C. H. 1952. Water movements in lakes during summer stratification: Evidence from the distribution of temperature in Windemere. Phil. Trans. R. Soc. Lond. A Math. Phys. Sci. **236:** 355–404.

PEDLOSKY, J. 1987. Geophysical fluid dynamics, 2nd ed. Springer.

SAGGIO, A., AND J. IMBERGER. 1998. Internal wave weather in a stratified lake. Limnol. Oceanogr. **43:** 1780–1795.

THOMSON, SIR W. (LORD KELVIN). 1879. On gravitational oscillations of rotating water. Proc. R. Soc. Edinb. **10:** 92–100.

THORPE, S. A., A. HALL, AND I. CROFTS. 1972. The internal surge in Loch Ness. Nature. **237:** 96–98.

TURNER, J. S. 1973. Buoyancy effects in fluids. Cambridge.